Supplement of Weather Clim. Dynam., 6, 1365–1378, 2025
https://doi.org/10.5194/wcd-6-1365-2025-supplement

Supplement of

Drivers and impacts of westerly moisture transport events in East Africa

Robert Peal and Emily Collier

Correspondence to: Robert Peal (robert.peal@uibk.ac.at)

S1 Sensitivity of WMTE detection to parameter choices

The WMTE detection algorithm has three free parameters: the magnitude threshold, the direction filter applied to each grid point, and the minimum size of detected objects. To select parameter values and understand the impact of parameter choice on the model, we ran the WMTE detection algorithm with different combinations of these parameters. We varied the magnitude threshold from 60% to the atmospheric river threshold of 85% from Guan and Waliser, 2015, upon which our method is based; the direction threshold by 10% around 45°; and, the size threshold from 750 to 1000 pixels. We ran the detector with all combinations of these parameters, resulting in a total of 36 runs. The parameter values tested are shown in table S1.

Table S1: The parameter values used in the sensitivity analysis

Magnitude threshold	60, 70, 80, 85
Direction threshold	40.5, 45, 49.5
Minimum size	750, 1000, 1500

To study the impact of parameter choice on EEA westerlies, we compare the statistics of events crossing the EEA line (29°E, 2°N to 12°S) for the different combinations. The percentage change in basic statistics when we change the parameter values from magnitude threshold=70%, direction threshold=45°, size threshold=1000 are shown in Figure S1. On each plot, the colour of the line represents the minimum size, and the line style represents the direction, so that following a single line shows the effect of changing the magnitude threshold for constant direction and size.

Figure S1a shows the effect of parameter choice on the number of WMTE polgons per month crossing the EEA line. For all combinations of the other parameters, the number of days decreases as the magnitude threshold increases, as would be expected. The decrease is roughly linear, but the rate increases for thresholds above 70%. The number of days per month increases with increasing values of the direction filter and with decreasing values of the size filter, but the lines are all relatively close together, showing that there is less sensitivity to these parameters.

We also show the statistics of 'events': periods of consecutive days where there was a WMTE crossing the EEA line. Figure S1b shows the average number of events per month, which shows similar patterns to those in the number of days per month, but the gradient is more constant and only steepens above a threshold of 80%. Figure S1c shows the mean length of events. The lines in this plot are more clustered and have a shallower gradient, showing that mean duration was less sensitive to parameter change. For all configurations, the gradient steepens above a magnitude threshold 70% and then becomes shallower above 80% apart from for configurations with size filter=1500. Since the median (Fig. S1d) can only take integer values, its behaviour is less consistent. The number of WMTE days normally decreased with the magnitude threshold, but with a size filter of 750 km, the number of WMTE days initially increased up to a threshold of 70% before decreasing again. Furthermore, while on the other plots, larger direction thresholds almost always lead to increases, increasing the direction filter often lead to decreases in the median length, showing that the days removed by these changes were usually part of longer events.

The patterns show that the increase in sensitivity of days per month to magnitude threshold above 70% (Fig. S1a) is due to days in long events being filtered out, leading to a reduction in the typical length of events (Fig. S1c). Increasing the magnitude threshold above 80% favours the exclusion of days in shorter events more strongly than in longer events, resulting in a sharper decrease in the typical number of events (Fig. S1b) but a stabilisation of the typical length (Fig. S1c).

To quantify the sensitivity, we have calculated the response of each statistic to 10% increase in each variable, while holding the other variables constant. To do this we have performed a linear regression of the percentage change of each statistic along each of the different parameter values, using parameter values as percentage changes relative to magnitude threshold=70%, direction threshold=45°, size threshold=1000. We have used these slopes to calculate the percentage change of the statistic under a 10% change in the parameter value. We display these as box plots in Fig. S2. Each point in the box plot is the sensitivity using the gradient with a certain combination of the other parameters. For example, each point in the magnitude threshold boxplot is the gradient of one of the lines in Fig. S1, which have constant values of direction and size. We then did the same for the other parameters.

Figure S2a–b shows that, consistent with Fig. S1, both the total WMTE days per month and event count per month were most sensitive to magnitude threshold: a 10% increase in the magnitude threshold decreased the statistics by around 26–28%, while a 10% increase in direction or size filter resulted in only around a 3–5% increase or a 2.5% decrease respectively in the value of either of the statistics. Mean duration (Fig. S2c) was less sensitive: a 10% increase in size had almost no effect, and the 10% increase in magnitude lead to around a 7% decrease in mean duration. The effect of increasing the direction 10% was just above 0 for most parameter sets, but a few

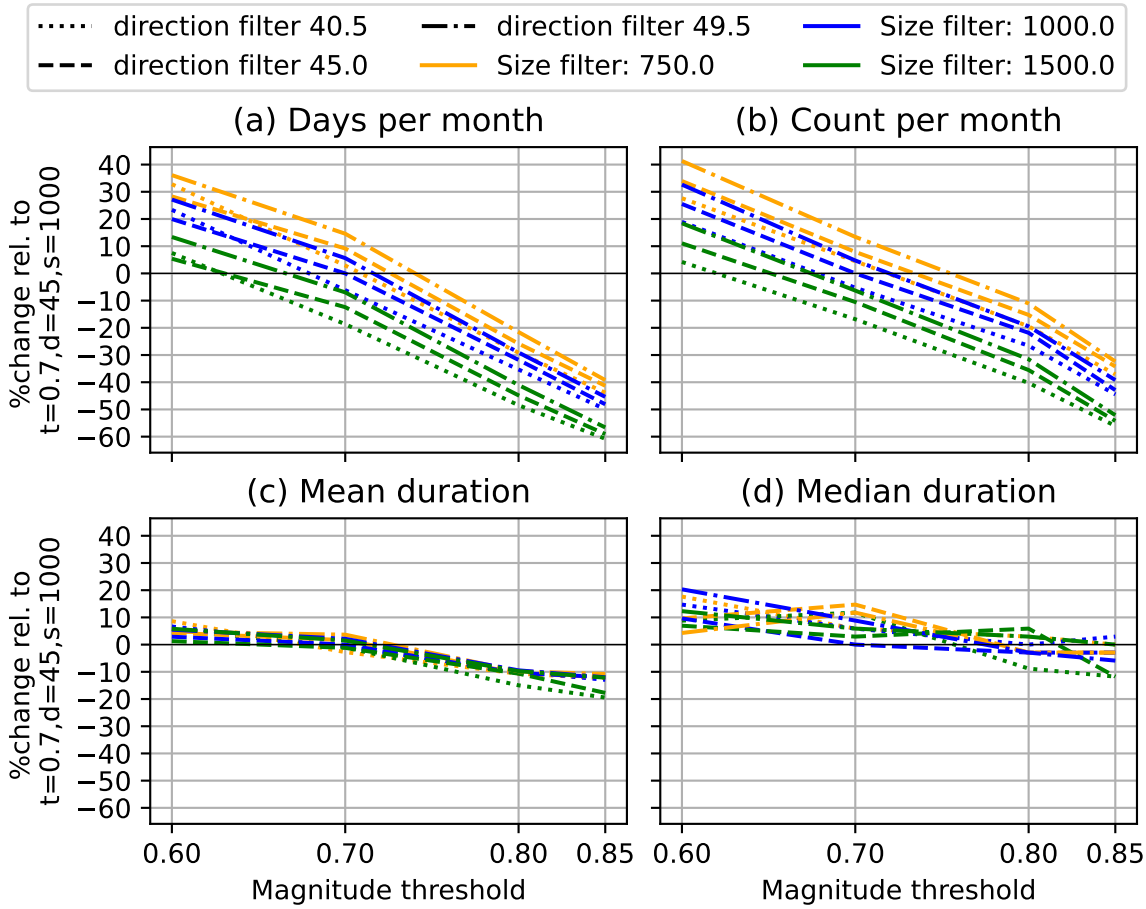

Figure S1: Statistics of WMTEs crossing the EEA line for different parameter combinations. The y axis shows the percentage change relative to the run with direction= 45°, size=1000 pixels, magnitude threshold=70%. **(a)** number of WMTE days per month, **(b)** count of WMTEs per month, **(c)** mean duration of WMTEs, **(d)** median duration of WMTEs.

combinations reduced the mean duration, reflecting the possibility of adding short events to the set. Similar but more exaggerated patterns were observed in the median duration (Fig. S2d), where sensitivity to direction and size was again very small but the direction was split almost evenly. Increases in the magnitude threshold still caused a decrease, of about 5–6%.

Due to the extremely low sensitivity of the method to size threshold, we settled on a value of 1000 grid points because it was a convenient number that excluded the smallest areas of westerly transport that are less interesting. The model is slightly more sensitive to the direction, but given even in the peak WMTE season of JF, there were only around 10 days per year with a WMTE in EEA, the sensitivity of a few percent is relatively small. We settled on 45° since it is easy to argue that we are interested in vectors within 45° of due west when investigating westerly events.

Clearly, the choice of magnitude threshold is the most important. 70% is lower than the typical atmospheric river threshold, but since EEA is often affected by strong easterlies, we didn't want to exclude westerly days of reasonable magnitude from locations with high magnitude easterly transport. We opted for 70% because it is still high enough to exclude days with only weak westerly transport, but is more generous than the AR threshold, and in particular allowed us to capture long duration events (Fig. S1c) that may be important for allowing moisture to travel into EEA from the Congo basin.

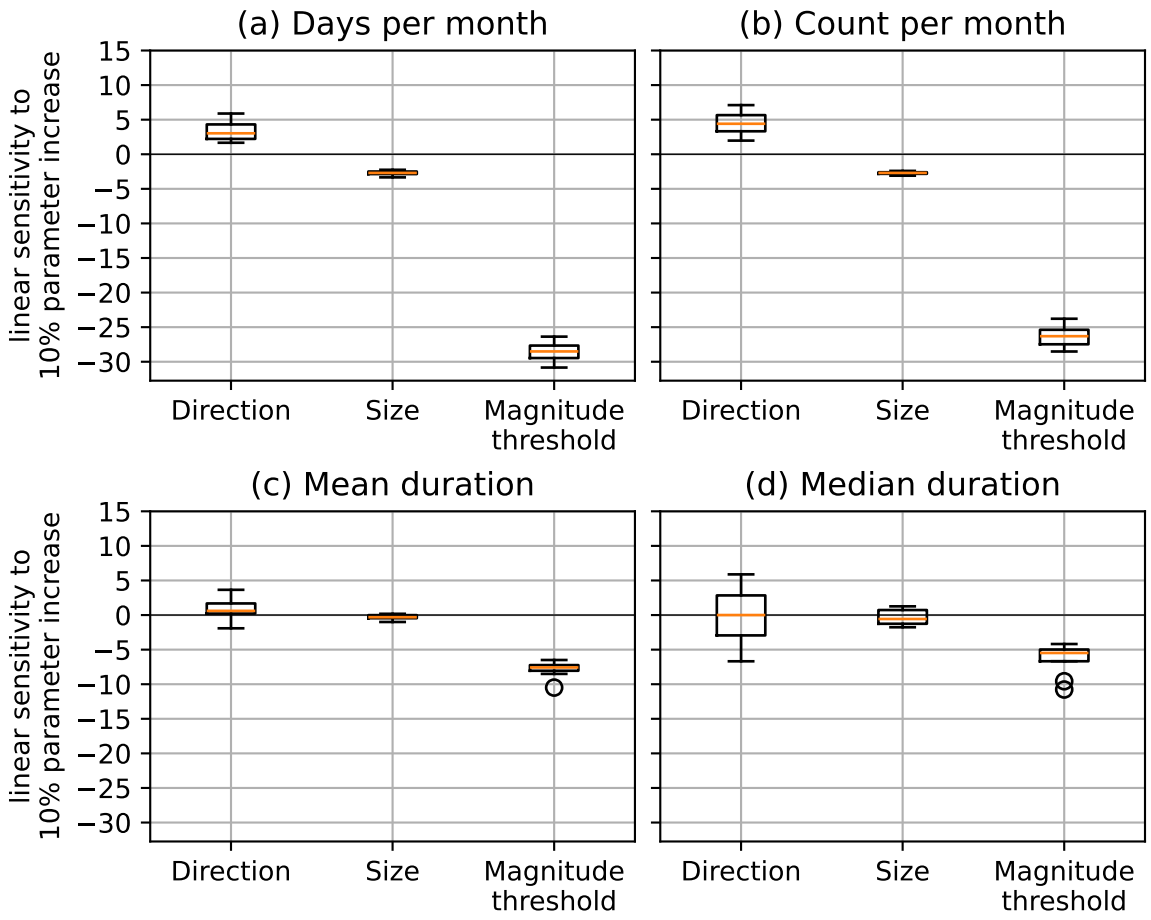

Figure S2: Sensitivity of statistics of WMTE polygons crossing the EEA line to a 10% parameter increase, when the other two parameters are held constant. Each datapoint contributing to the box plots represents one unique combination of the other two parameters. **(a)** the change in number of WMTE days per month when direction/size/threshold change by 10%, **(b)** same for count of WMTEs per month, **(c)** same for mean duration of WMTEs, **(d)** same for median duration of WMTEs. Points beyond the end of the whiskers are plotted.

S2 Example detections

We show more example detections to provide more insights into the algorithm. To illustrate how the method describes notable precipitation events, Fig. S3 shows the WMTEs detected during a period of high precipitation in the anomalously wet long rains of 2018. The event develops on 2018-03-10, and is designated as a TC-WMTE on 2018-03-13 due to the formation of tropical cyclone Dumazile east of Madagascar.

We also show some more diverse examples of detection in Fig. S4. Here we discuss some general properties of these detections and highlight some possible shortcomings of the method.

- Events had considerable variation in latitudinal and longitudinal extent. Some events were extremely wide (e.g. Fig. S4a), while others were narrower (e.g. Fig. S4b). Events usually extended into the Indian ocean and some events extended westwards over the eastern edge Atlantic Ocean (e.g. Fig. S4b).

- The very rare detections in JJAS tended to be unstructured objects, often appearing as a patchwork of areas of westerly transport (e.g. Fig. S4c, d). However, such configurations were extremely rare in the main months of interest in this study.

- The thresholding approach means that what may be single events were sometimes split into separate entities (e.g. Fig. S4e, f). A single WMTE over EEA on 1999-12-14 (Fig. S4e) splits into two objects on 1999-12-15 (Fig. S4f). In this case, the larger event over EEA has more overlap, and so is tracked as part of the same WMTE, but the separate region is a new, independent WMTE starting on 1999-12-15. It appears the object was split because there was a region where the transport was not within $\pm 45^{\circ}$ of westerly.

- Some examples (e.g. Fig. S4a and f show that when multiple WMTE polygons were detected and/or when other convective systems like TCs were present, the precipitation attributed using the method of (Konstali et al., 2024) extends well beyond the edge of the WMTE mask. In the case of Fig. S4f, the extension seems physically reasonable since the gap between the two WMTEs still has strong northwesterly transport, and so using this method may help to offset cases where the thresholding was too strict.

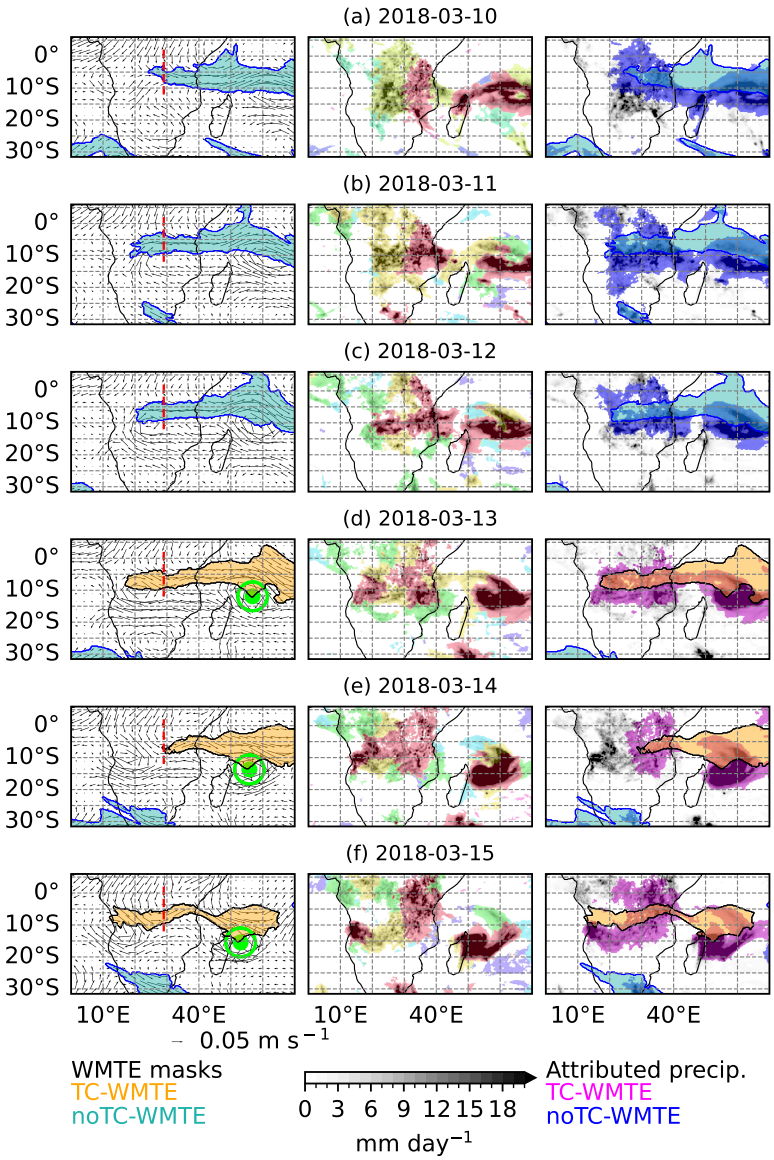

Figure S3: Example detections during the anomalous long rains of 2018. Each row shows an individual date. The left panel shows the 700 hPa moisture transport field, with WMTE masks shaded in light blue and TC-WMTE masks shaded in orange. The middle panel shows the ERA5 precipitation and the masks of the precipitation objects. The right panel shows the WMTE objects, and precipitation attributed to TC-WMTEs in pink and to WMTEs in blue.

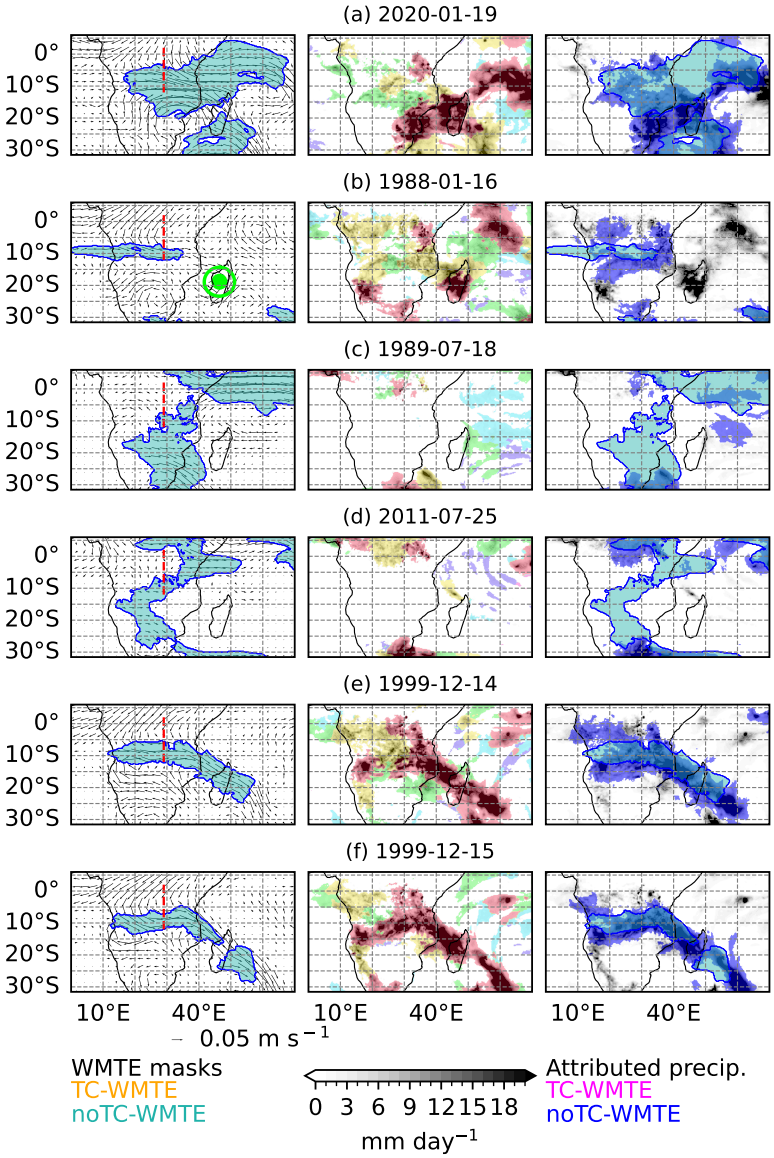

Figure S4: Same as Fig. S3 for some other detection examples.

S3 Sensitivity to the 500-km TC-distance threshold

We also investigated the sensitivity of the distance threshold for TC-WMTEs by varying it from 250 to 750 km (Fig. S5). The percentage of WMTE polygons crossing the EEA line that were TC-WMTE polygons was relatively insensitive. For example, in January and February, the months with the highest number of WMTEs crossing the EEA line, changing the distance threshold from 250 to 750 km changed the percentage of those polygons classified as TC-WMTE polygons from approximately 38% to 41%.

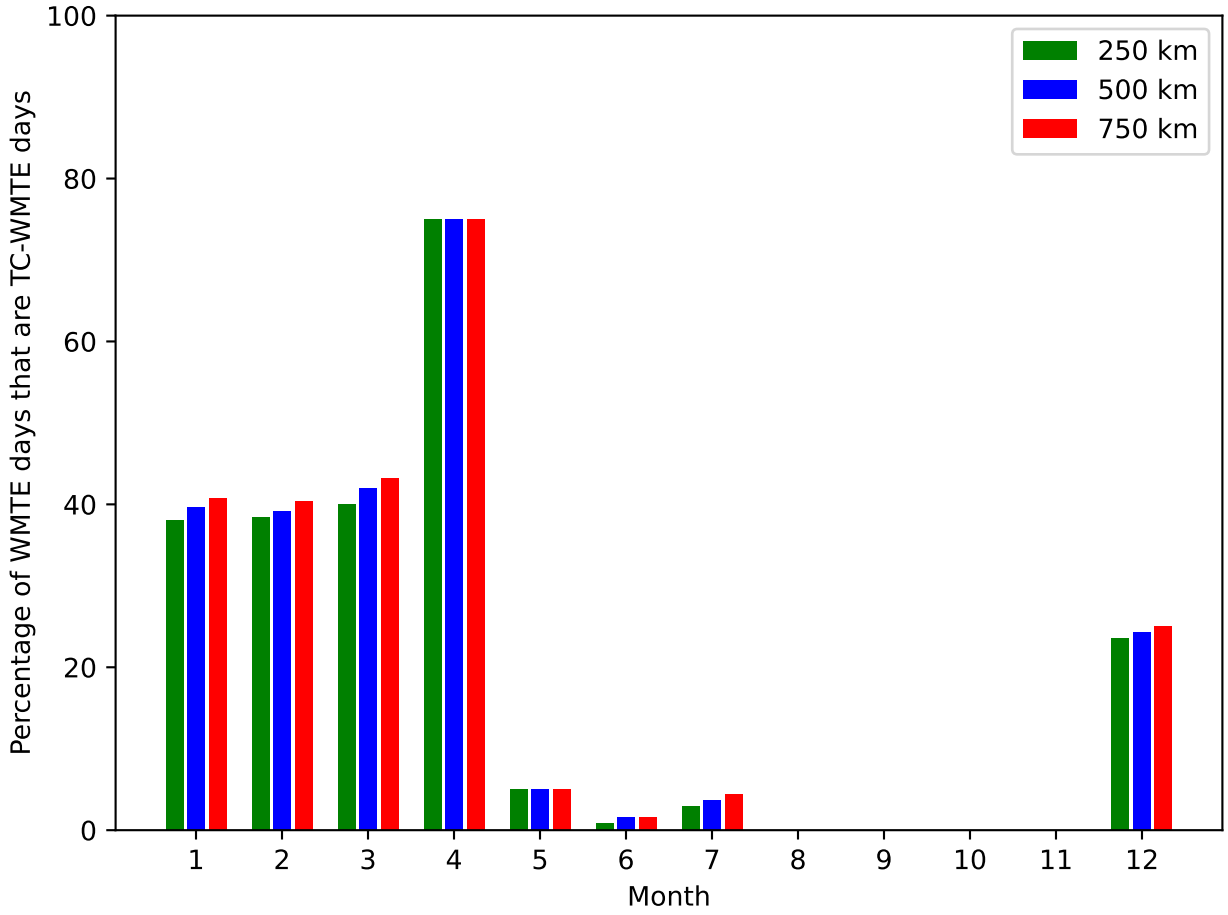

Figure S5: The percentage of days with a WMTE polygon crossing the EEA line where the polygon was located within the distance threshold of a TC.

S4 Precipitation attribution using conservative approach

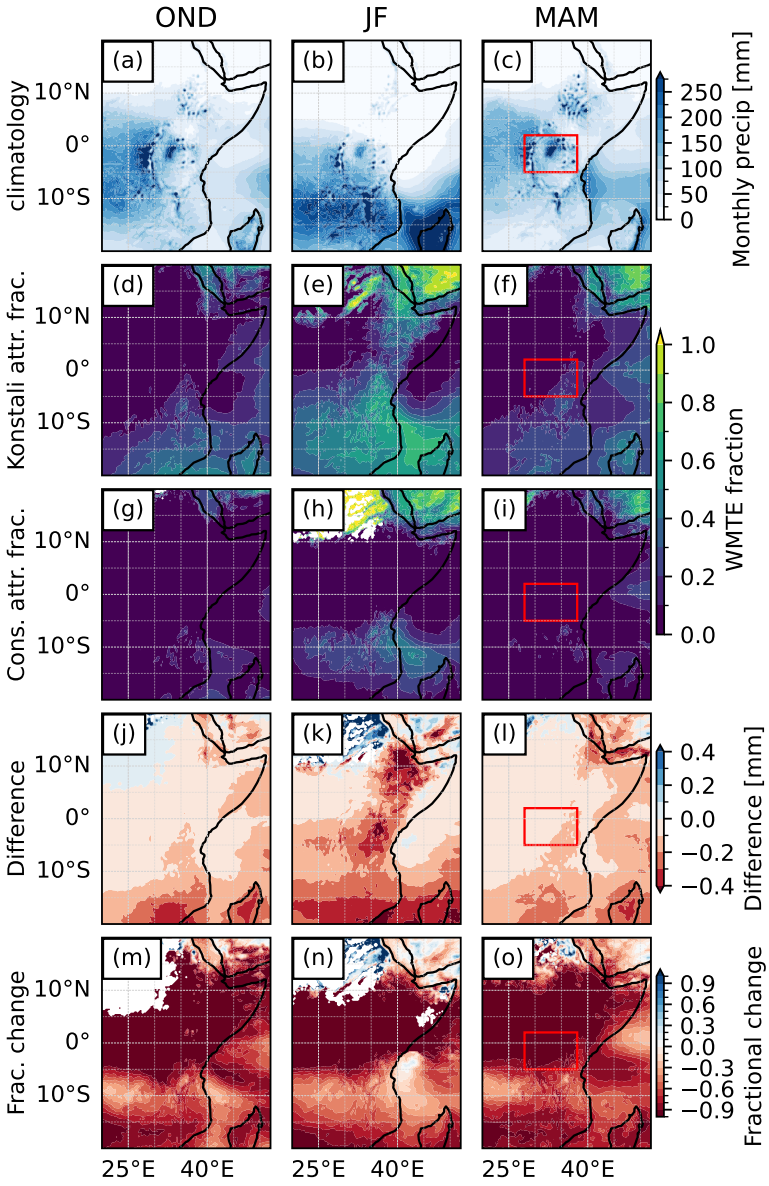

Figure S6: (a–c) The ERA5 average monthly precipitation from 1998 to 2022 for the seasons of OND, JF and MAM. (d–f) The fraction of precipitation that was attributed to WMTEs in each season using the method of (Konstali et al., 2024). (g–i) The fraction of precipitation directly inside WMTE masks. (j–l) The difference between the two approaches. (m–o) The fractional change between the two approaches. We note that small increases in the amount of attributed precipitation in some very dry areas are due to removing the wet day threshold for the conservative approach.

S5 Duration of TC- and noTC-WMTEs

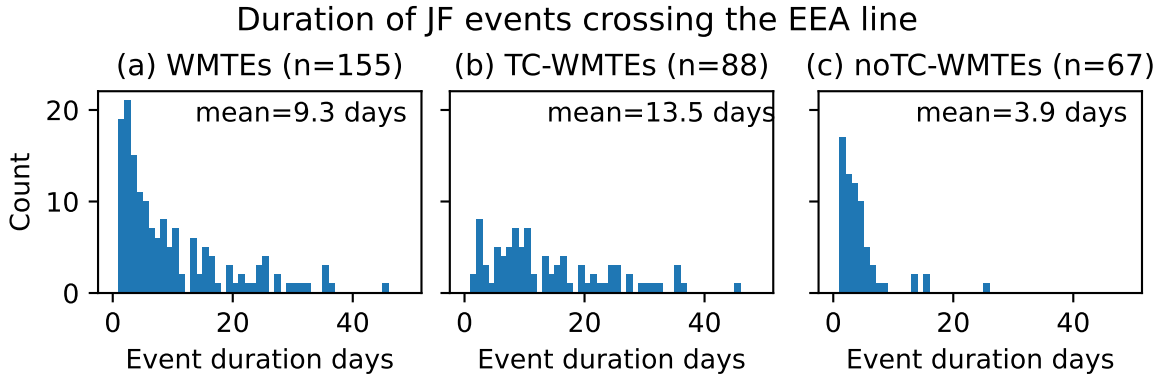

Figure S7: Histograms showing the duration of events that started in JF and crossed the EEA line on at least one day during the event, for TC-WMTEs (events that were within 500 km of a TC on at least one day) and noTC-WMTEs (events that were never within 500 km of a TC).

S6 Moisture transport at 850 hPa during WMTEs

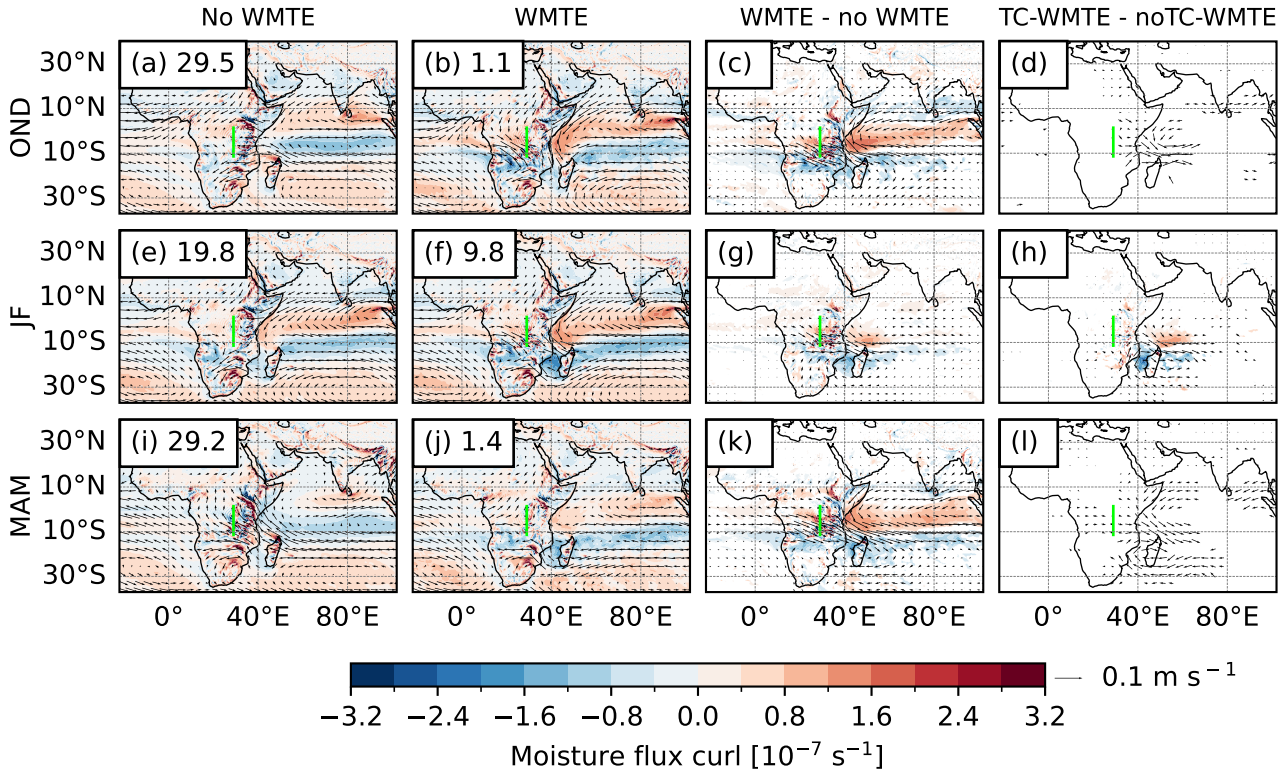

Figure S8: Same as Fig. 3 in main text, but for 850 hPa level. Composites of 850-hPa moisture transport in **(a–d)** OND, **(e–h)** JF, and **(i–l)** MAM. **(a, e, i)** Days without a WMTE polygon crossing the EEA line (2° N–12° S along 29° E), shown by the green line. **(b, f, j)** Days with a WMTE polygon crossing the EEA line. **(c, g, k)** Difference between the composite of days with, and without, a WMTE polygon crossing the EEA line. **(d, h, l)** Difference between the composite of days with a TC-WMTE, and days with a noTC-WMTE, polygon crossing the EEA line. The shading represents the curl of the moisture transport field. The numbers labelled in the first two columns show the average number of days per month in that composite. Differences are shown only where they were significant at the 95% level using a permutation test with 1000 permutations.

S7 Risk ratio of WMTE occurrence in other seasons

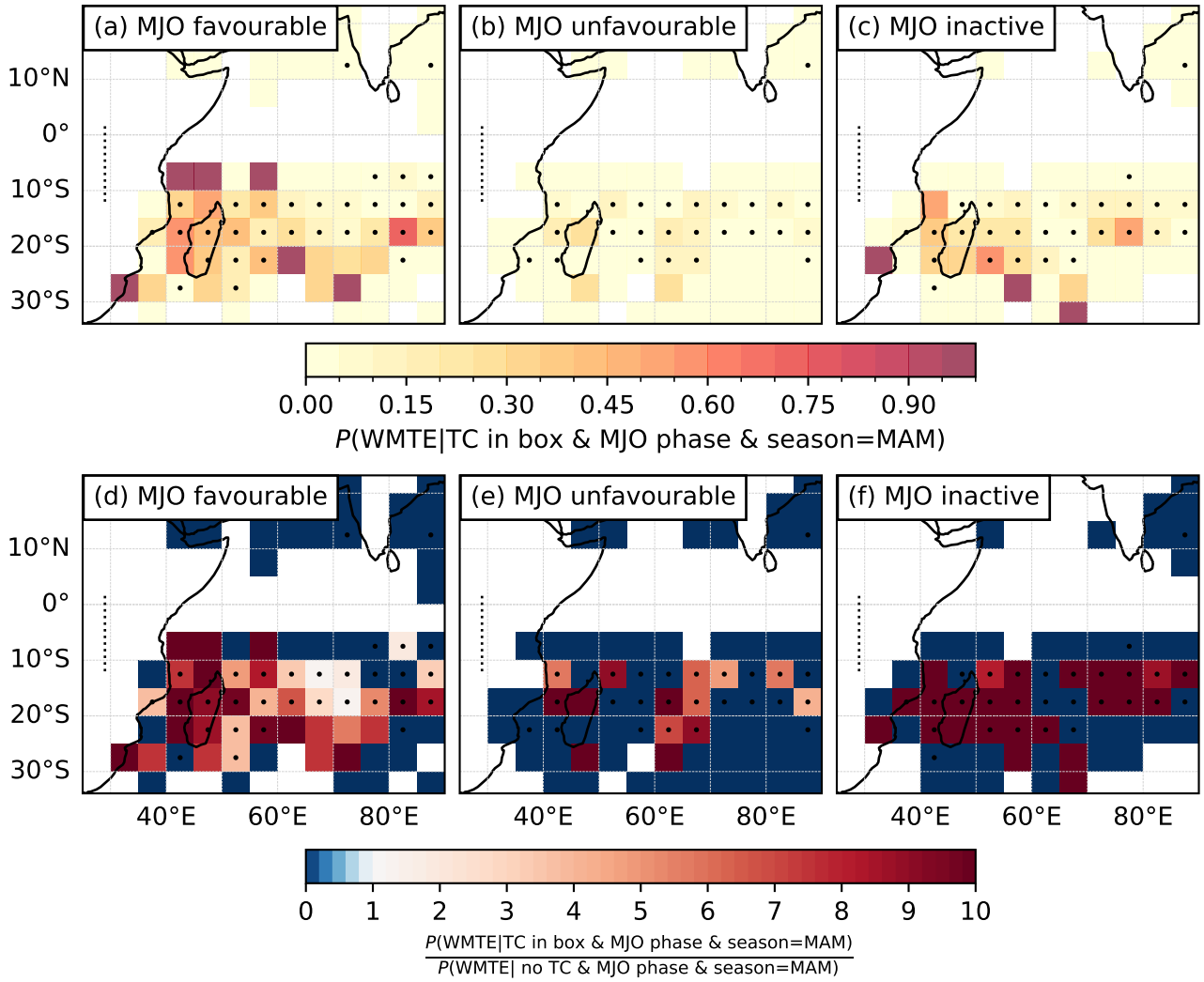

Figure S9: Same as Fig. 5 in main text, but all panels show MAM. How the presence of a TC at different locations changes the probability of a WMTE day in EEA. **(a–c)** The probability of a WMTE crossing the EEA line, shown by the black dashed line, given the presence of a TC in 5° grid boxes, during MAM. **(d–f)** MAM relative risk for each box, showing the ratio of the probability of a WMTE crossing the line given the presence of a TC, compared to the probability of a WMTE crossing the line, given there is no TC anywhere in the Indian Ocean. Boxes with a dot have at least five TC reports in the period 1980–2022. **(a, d)** MJO phases 2–4, **(b, e)** MJO phases 5–1, **(c, f)** MJO inactive.

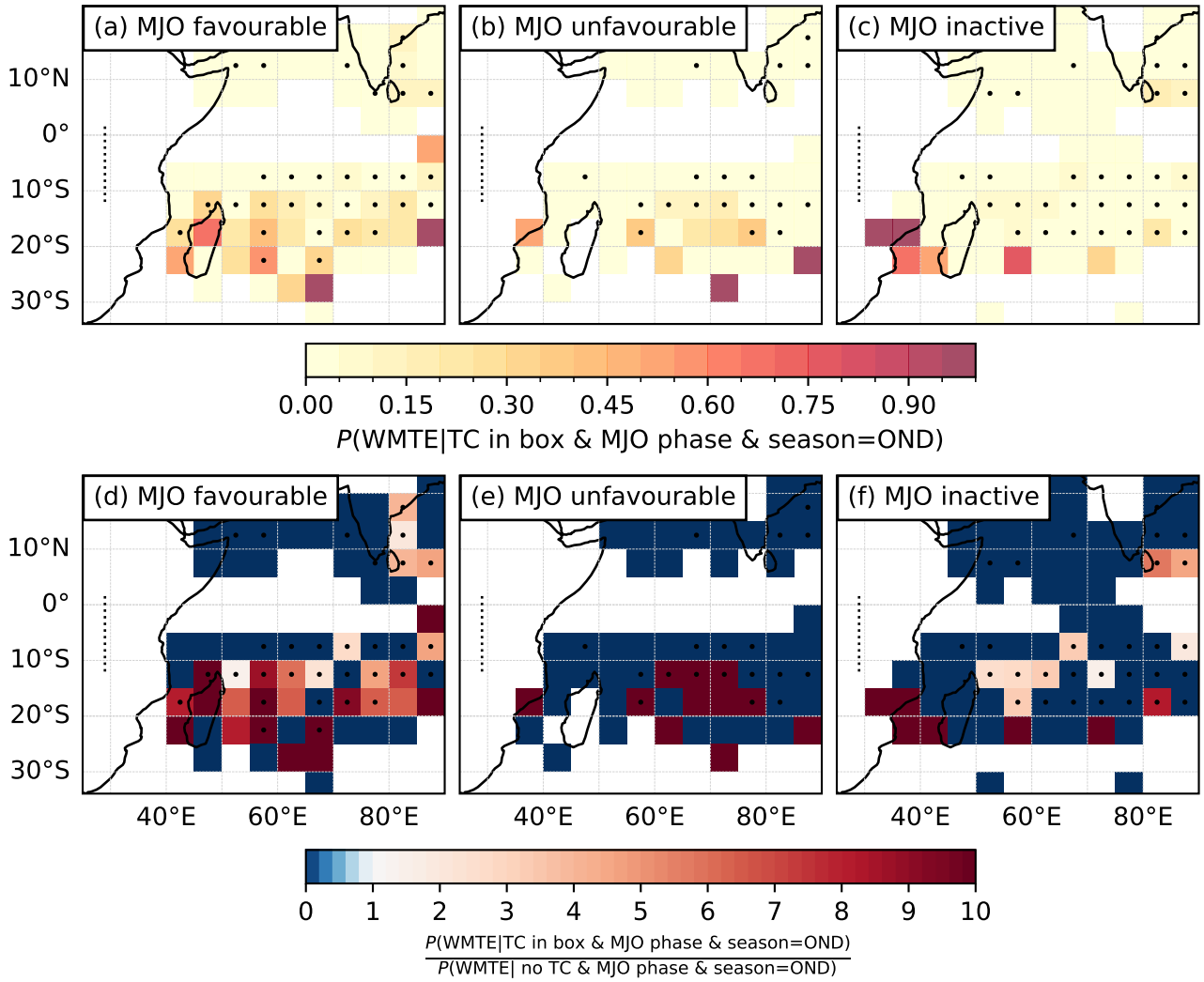

Figure S10: Same as Fig. 5 in main text, but all panels show OND. How the presence of a TC at different locations changes the probability of a WMTE day in EEA. **(a–c)** The probability of a WMTE crossing the EEA line, shown by the black dashed line, given the presence of a TC in 5° grid boxes, during OND. **(d–f)** OND relative risk for each box, showing the ratio of the probability of a WMTE crossing the line given the presence of a TC, compared to the probability of a WMTE crossing the line, given there is no TC anywhere in the Indian Ocean. Boxes with a dot have at least five TC reports in the period 1980–2022. **(a, d)** MJO phases 2–4, **(b, e)** MJO phases 5–1, **(c, f)** MJO inactive.

S8 TC occurrence during TC-WMTEs

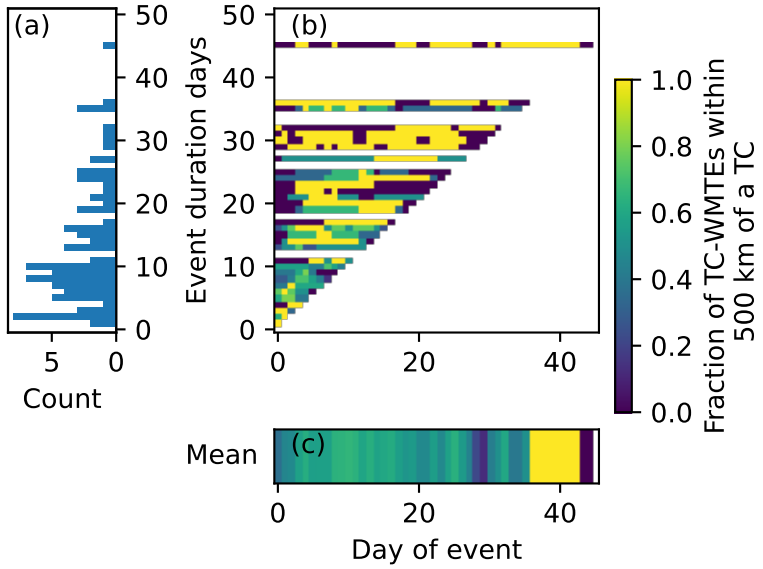

Figure S11: (a) Histogram showing the number of TC-WMTEs that started in JF and crossed the EEA line on at least one day, compared with their total lifetimes. (b) The fraction of the TC-WMTEs in (a) with a given duration that were within 500 km of a TC, considering each successive day of the event. (c) The average over all event durations shown in (b).

We note that the unusual longer events shown in Fig. S11, such as the one that persisted for 45 days from 2000-01-28 to 2000-03-12, affected EEA for only a few days at a time, and were rather mostly located over the central Indian Ocean.

S9 Precipitation dataset comparison

S9.1 ERA5 1998–2022

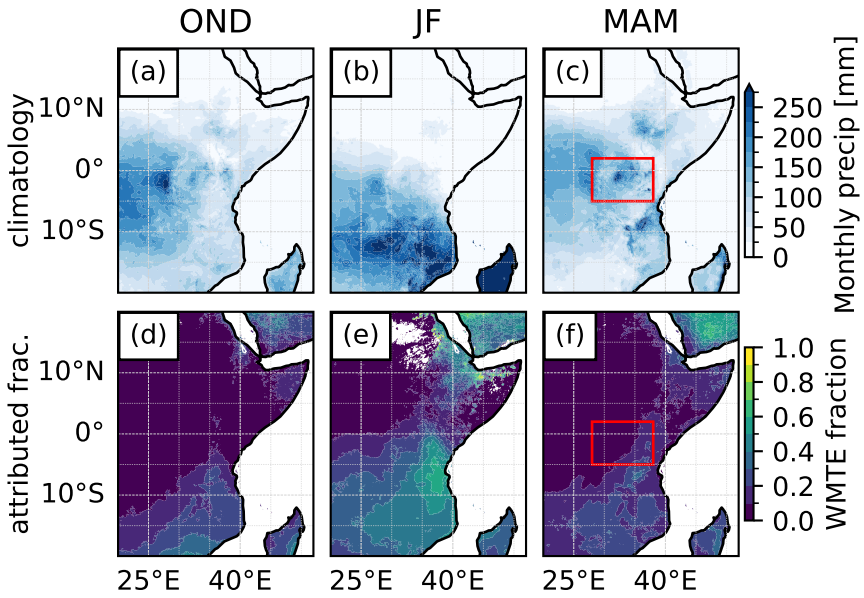

Figure S12: (a–c) The ERA5 average monthly precipitation from 1998 to 2022 for the seasons of OND, JF and MAM; (d–f) The fraction of precipitation that was attributed to WMTEs in each season.

S9.2 CHIRPS 1998–2022

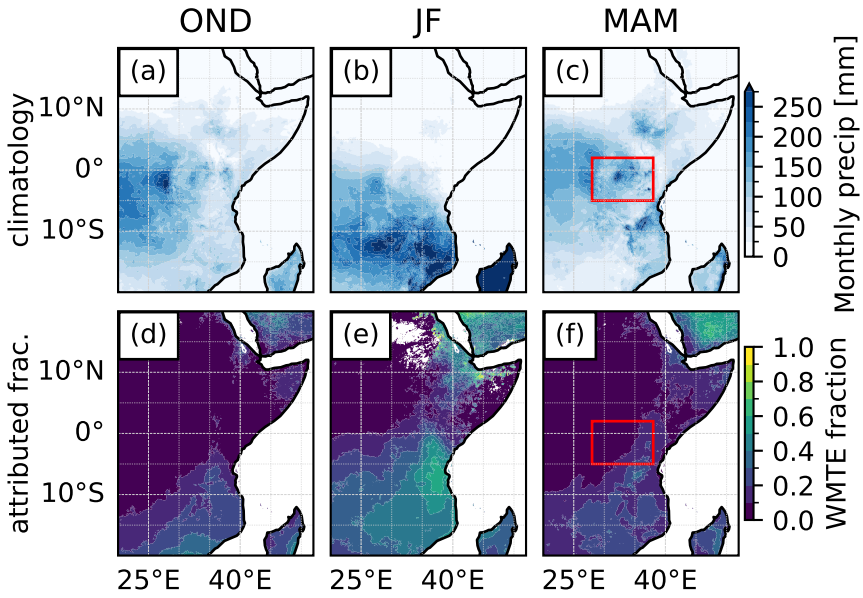

Figure S13: (a–c) The CHIRPS average monthly precipitation from 1998 to 2022 for the seasons of OND, JF and MAM; (d–f) The fraction of precipitation that was attributed to WMTEs in each season.

S9.3 IMERG 1998–2022

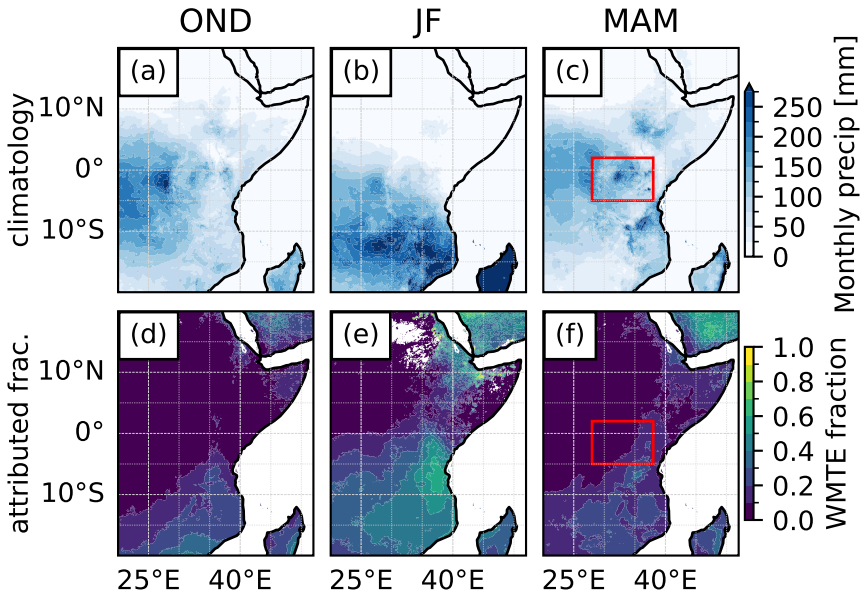

Figure S14: (a–c) The IMERG average monthly precipitation from 1998 to 2022 for the seasons of OND, JF and MAM; (d–f) The fraction of precipitation that was attributed to WMTEs in each season.

S10 WMTEs properties and their impact on precipitation

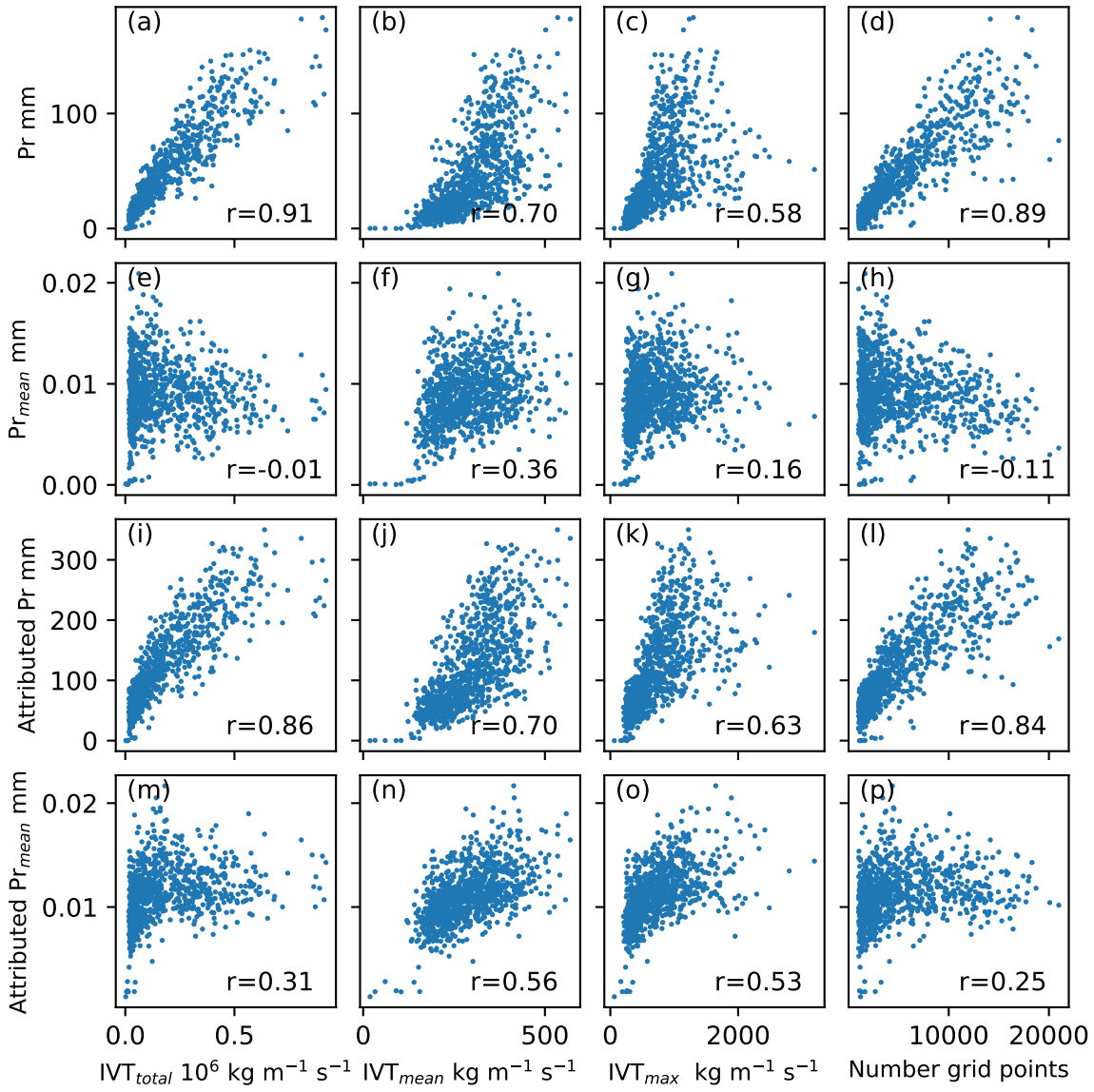

Figure S15: Metrics describing WMTEs and their relationship to precipitation. Each point represents a day where there was a WMTE crossing the EEA line. Precipitation metrics: (a–d) Total and (e–h) mean precipitation directly inside the WMTE polygon. (i–l) Total and (m–p) mean precipitation attributed to the WMTE. WMTE properties: (a, e, i, m) Total, (b, f, j, n) mean, and (c, g, k, o) max IVT inside the WMTE polygon; and, (d, h, l, p) area of the WMTE polygon. Each plot includes the Pearson correlation coefficeint.

References

Guan, B. and D. E. Waliser (2015). "Detection of atmospheric rivers: Evaluation and application of an algorithm for global studies". In: *Journal of Geophysical Research: Atmospheres* 120.24, pp. 12514–12535. DOI: https://doi.org/10.1002/2015JD024257.

Konstali, K. et al. (2024). "Global Attribution of Precipitation to Weather Features". In: *Journal of Climate* 37.4, pp. 1181–1196. DOI: 10.1175/JCLI-D-23-0293.1. URL: https://journals.ametsoc.org/view/journals/clim/37/4/JCLI-D-23-0293.1.xml.